Progranulin-dependent repair function of Regulatory T cells drive bone fracture healing

Ruiying Chen[1], Xiaomeng Zhang[1], Bin Li[2], Maurizio S Tonetti[1], Yijie Yang[1], Yuan Li[1], Beilei Liu[1], Shujiao Qian[1], Yingxin Gu[1], Qingwen Wang[3], Kairui Mao[4], Hao Cheng[5], Hongchang Lai[1], Junyu Shi[1]

1. Department of Oral and Maxillofacial Implantology, Shanghai PerioImplant Innovation Center, Shanghai Ninth People's Hospital, Shanghai Jiao Tong University School of Medicine; College of Stomatology, Shanghai Jiao Tong University; National Center for Stomatology; National Clinical Research Center for Oral Diseases; Shanghai Key Laboratory of Stomatology; Shanghai Research Institute of Stomatology, Shanghai, China.
2. Center for Immune-Related Diseases at Shanghai Institute of Immunology, Department of Respiratory and Critical Care Medicine of Ruijin Hospital, Department of Thoracic Surgery of Ruijin Hospital, Department of Immunology and Microbiology, Shanghai Jiao Tong University School of Medicine, Shanghai, China; Department of Integrated TCM & Western Medicine, Shanghai Skin Disease Hospital, School of Medicine, Tongji University, Shanghai, China; Department of Thoracic Surgery, Shanghai Pulmonary Hospital, Tongji University, Shanghai, China; Department of Oncology, Department of Hepatobiliary Surgery, The First Affiliated Hospital of Anhui Medical University, Hefei, China.
3. Shenzhen Key Laboratory of Immunity and Inflammatory Diseases, Shenzhen, Guangdong, China; Department of Rheumatism and Immunology, Peking University Shenzhen Hospital, Guangdong, China.

4. State Key Laboratory of Cellular Stress Biology, Innovation Center for Cell Signaling Network, School of Life Sciences, Xiamen University, Xiamen, China.
5. Center for Immune-Related Diseases at Shanghai Institute of Immunology, Department of Respiratory and Critical Care Medicine of Ruijin Hospital, Department of Thoracic Surgery of Ruijin Hospital, Department of Immunology and Microbiology, Shanghai Jiao Tong University School of Medicine, Shanghai, China; Department of Rheumatism and Immunology, Peking University Shenzhen Hospital, Guangdong, China; Center for Cancer Immunology Research, Shenzhen Institutes of Advanced Technology, Chinese Academy of Sciences, Shenzhen, Guangdong, China.

Address correspondence to: Junyu Shi, Department of Oral and Maxillofacial Implantology, Shanghai Ninth People's Hospital, 639 Zhizaoju Road, Huangpu District, Shanghai, China. Phone: 86.021.53315299. Email: sjy0511@hotmail.com. Or to Hongchang Lai: Department of Oral and Maxillofacial Implantology, Shanghai Ninth People's Hospital, 639 Zhizaoju Road, Huangpu District, Shanghai, China. Phone: 86.021.53315299. Email: laihongchang@sjtu.edu.cn. Or to Hao Cheng: Department of Immunology and Microbiology, Shanghai Jiao Tong University School of Medicine, 208 Chongqingnan Road, Huangpu District, Shanghai, China. Phone: 86.15022599429. Email: chenghaowj@alumni.sjtu.edu.cn.

Authorship note: RC and XZ contributed equally to this work and are co–first authors. JS, HL and HC contributed equally to this work and are co–senior authors.

Conflict of interests: The authors have declared that no conflict of interest exists.

Abstract

Local immunoinflammatory events instruct skeletal stem cells (SSCs) to repair/regenerate bone after injury, but mechanisms are incompletely understood. We hypothesized that specialized Regulatory T (Treg) cells are necessary for bone repair and interact directly with SSCs through organ-specific messages. Both in human patients with bone fracture and mouse model of bone injury, we identified a bone injury-responding Treg subpopulation with bone-repair capacity marked by CCR8. Local production of CCL1 induced a massive migration of $CCR8^+$ Treg cells from periphery to the injury site. Depending on secretion of progranulin (PGRN), a protein encoded by the granulin (*Grn*) gene, $CCR8^+$ Treg cells supported the accumulation and osteogenic differentiation of SSCs, and thereby bone repair. Mechanistically, we revealed that CCL1 enhanced expression level of basic leucine zipper ATF-like transcription factor (BATF) in $CCR8^+$ Treg cells, which bound to *Grn* promoter and increased *Grn* translational output and then PGRN secretion. Together, our work provides a new perspective in osteoimmunology and highlights possible ways of manipulating Treg cell signaling to enhance bone repair and regeneration.

Introduction

Bone fractures are a serious public health issue due to their high prevalence and serious consequences (178 million cases in 2019) (1). They may heal with complications (non-union) and frequently require surgical intervention, especially in aging subjects. Bone repair depends on the highly coordinated mobilization, proliferation, and differentiation of skeletal stem cells (SSCs) and their progeny within the injury site (2, 3). After an injury, quiescent stem cells receive signals from the local environment to activate their bone repair function (3, 4). However, previous bone repair studies (5-7) were mainly performed with mesenchymal stem cells: a heterogeneous cell population with varying differentiating potential and including cells from other lineages rather than uniform purified skeletal stem cells. Thus, knowledge of the exact cues within the local environment instructing SSCs toward bone repair is limited. Recently, through a combination of fluorescence-activated cell sorting (FACS) and lineage reporter mice, highly purified SSCs, the highly selective and homogeneous cell population responsible for bone organ development, growth, and regeneration/repair, have been identified (8, 9). This enables direct investigation of the instructing mechanism of SSCs function during bone repair.

After bone injury, immune cells first trigger inflammation and later produce the necessary anti-inflammatory signals that allow SSCs to initiate bone repair (10, 11). Besides the established roles of macrophages and neutrophils (5, 12, 13), multiple lines of evidences point to a possible role of Treg cells in bone repair and homeostasis (14-16).

Decreased Treg cells accumulation has been observed in patients with non-healing fractures (17-20), like AIDS patients (19, 20). Additionally, Parathyroid Hormone (PTH)-induced bone formation was impaired by Treg cell ablation (21, 22). The mechanism(s) of these observations have yet to be elucidated, and it is unclear if Treg cells can directly affect SSCs function.

In addition, Treg cells are a vital component of the tissue stem-cell niche (23, 24): they support stem cell function, maintain tissue homeostasis, and promote tissue repair in multiple organs, including lung (25), cardiac muscle (26, 27), skeletal muscle (28), skin (29), and brain (30). The bone marrow is also a known reservoir for Treg cells (14).

We hypothesized that Treg cells are necessary for bone repair and interact directly with SSCs. Through using a mouse model of bone injury and combined with single-cell RNA sequencing (scRNA-seq) of intramedullary canal tissue samples obtained from human patients with bone fracture (31), we showed that bone repair required the accumulation of a unique Treg subpopulation with bone repair signature and marked by CCR8 at the injury site. These cells secreted progranulin (PGRN), encoded by the granulin (*Grn*) gene, to promote SSCs accumulation, osteogenic differentiation and then bone repair. Moreover, local production of CCL1 recruited the $CCR8^+$ Treg cells from periphery to the injury site and promote their secretion of PGRN through enhanced transcriptional activity of *Grn* induced by basic leucine zipper ATF-like transcription factor (BATF). Collectively, our study elucidated an immune-related bone repair mechanism mediated by $CCR8^+$ Treg cells.

Results

1. Treg cells accumulate at the bone injury site and are required for bone repair

We firstly observed Treg cells' involvement in bone healing after standardized drill-hole surgery in the femur. During the bone repair process (Supplemental Figure 1A), Treg cells significantly accumulated at the injury site, as indicated by more abundant positive staining of FOXP3-GFP from 3 days after surgery (Figure 1A, Supplemental Figure 1B). Flow cytometry analysis of the cells harvested from the wound/callus tissue (including nearby bone marrow (BM)) (Figure 1B-C, Supplemental Figure C-D) showed that the proportions of Treg cells in the injury tissue increased from day 3 post-injury and peaked on day 7 when they accounted for 69.2 ± 7.5 % of the $CD4^+TCR\beta^+$ cells. The absolute number of Treg cells within the injury site also showed significant increasement on day 7, remained high and slowly returned to normal one month after injury. No significant changes in Treg cell proportions and numbers were observed in the spleen (SP) of the same mice over the time course (Figure 1B-C).

To verify the critical role of Treg cells in bone repair, we selectively depleted Treg cells by injecting diphtheria toxin (DT) into *Foxp3*-DTR (DT receptor) transgenic mice (Treg-depletion group) after bone injury (Figure 1D). Untreated *Foxp3*-DTR transgenic mice were used as Control group. Seven days after DT administration, over 85% of $CD4^+FOXP3^+$ cells were effectively depleted from the bone marrow compared to untreated *Foxp3*-DTR mice (Figure 1E-F). In the Treg-depletion group, safranin O staining revealed

the reduction of deposited bone matrix and cartilage tissue in the injury lesion on day 14 (Figure 1G-H). Hematoxylin and eosin (HE) staining results showed non-union with primarily fibrous tissue around the injury site in the Treg-depletion group on day 28, whereas the control group exhibited completed union (Figure 1I). We also verified the results in a femur fracture model in mice. In the Treg-depletion group, the absence of callus and non-union was observed, but in the controls, fracture healing was observed in all cases (Supplemental Figure 2).

As previous studies have indicated a tight relationship between Treg cells and osteoclasts (16, 32), we also evaluated if Treg cell depletion changed the numbers or distribution of osteoclasts in the bone marrow. Tartrate-resistant Acid Phosphatse (TRAP) staining showed no significant difference in the osteoclast number between the control and Treg-depletion groups (Supplemental Figure 3).

These results indicated that increased accumulation of Treg cells is required during bone repair.

2. Treg cells at the bone injury site are essential for promoting SSCs accumulation and osteogenic differentiation

We next studied the regulating effects of Treg cells on injury-associated SSCs, since Treg cells have been observed communicating with tissue stem cells (24). We firstly observed the injury-induced expansion and distribution of SSCs within the injury site from Treg-depleted mice and control mice. Previously reported surface markers of skeletal stem and

progenitor cells were used to distinguish skeletal stem cell subsets (8, 9) and their differentiation within the injury site (Figure 2A-B, Supplemental Figure S4). Flow cytometry analysis of the callus tissue showed an immediate increased accumulation of SSCs, bone, cartilage, and stromal progenitor cells (BCSPs) and mature osteo-lineage ($Thy1^{+}$) cells from day 7 and remained at high level in one month after bone injury (Figure 2B). These data indicated that SSCs accumulated in the callus immediately after injury and then were activated and gave rise to abundant skeletal progenitor cells and mature osteoblasts for bone repair. However, significant decreases in the percentages of total skeletal stem lineage cells, SSCs, BCSPs, and mature osteo-lineage cells were observed within the callus in the Treg-depletion group compared with control group (Figure 2B). These results indicated that injury-induced SSCs niche expansion was diminished under the Treg-depletion condition.

We also collected SSCs from callus tissues for bulk-RNA sequencing (seq) analysis. In control group, compared with SSCs from the uninjured bone tissues, SSCs from the injury sites displayed significant upregulation of genes related to stemness (e.g., *Ctsk*, *Sox9*, *Cd200*, and *Pdgfrb*) and osteogenic differentiation (e.g., *Alp*, *Ogn*, and *Runx2*). In the SSCs isolated from Treg-depleted mice, however, the expression of genes involved in stemness and osteogenesis was downregulated, while the expression of genes participating in apoptosis and senescence (e.g., *Casp4*, *Apaf1*, *Csf2ra*) was upregulated (Figure 2C). The Volcano plots (Figure 2D) also showed that the osteogenic differentiation genes expression

in SSCs was inhibited by Treg cells depletion. In addition, gene ontology (GO) term enrichment analysis of differentially expressed genes also confirmed that biological processes “stem cell differentiation”, “osteoblast differentiation”, and pathways “BMP signaling” and “TGF-β signaling” were more significantly enriched in SSCs from the injury site in control mice, while not enriched in Treg-depleted mice (Figure 2E).

We further isolated Treg cells from mouse spleens and lymph nodes and cultured *in vitro* for 3 days, and then the supernatant was collected. From the same mice, we also isolated SSCs and subjected them to a standard osteogenic/adipogenic differentiation assay in the presence or absence of supernatant collected from cultured Treg cells (Figure 2F). SSCs stimulated by the Treg supernatant showed significantly elevated osteogenic differentiation, revealed by increased alkaline phosphatase (ALP)-positive staining colonies (Figure 2G). The Oil red staining revealed no significant difference in their adipogenic differentiation ability (Figure 2G).

Given the DT toxicity, we also constructed bone injury model in DT treated wild type (WT) mice. And the results showed that DT itself didn’t affect the SSCs accumulation, function and bone healing after bone injury (Supplemental Figure 5). Together, these experiments demonstrated that the Treg-depletion reduced SSCs accumulation and impaired SSC osteo-lineage output during the injury repair process.

3. **Identification of an “injury-responding” Treg subpopulation with bone-repair capacity**

Treg cells have remarkable phenotypic plasticity and tissue specificity and can exhibit distinct features in response to a changing environment (33-35). Thus, we explored whether the bone injury niche imparts distinct features beneficial for bone repair to these Treg cells. Bull-RNA sequencing analysis showed upregulated transcripts in Treg cells isolated from injured bone tissue (Treg-injury cells) encoded Treg cells activation markers (e.g., *Ctla4*, *Il1r2* and *Tnf* receptor superfamily members) and effector molecules (e.g., *Gata3*, *Nfkbia* and *Klrg1*). Conversely, Treg-Injury cells made lower transcripts encoding proteins known to dampen the inflammation (e.g., *Ifng*, *Cxcr5* and *Il17a*) (Figure 3A). Flow cytometry analysis confirmed that significantly higher percentages of Treg-Injury cells expressed functional markers (CD44, CTLA and KLRG1) compared with the Treg-Cntrl cells and spleen Treg cells (Figure 3B). These data indicated that bone injury induced a significant phenotypic change of Treg cells at the injury site.

Furthermore, we performed a bioinformatics analysis using a scRNA-seq dataset of bone marrow cells from a previous study analyzing immune cells constitution in intramedullary canal tissue obtained from human fracture patients (31). For control group, the bone marrow tissue was obtained when harvesting autologous bone graft. In fracture group, bone marrow sample was collected when patients undergoing internal fixation of fracture. And bone marrow sample for non-union group was collected at the time of surgical repair for femur fracture non-union. Besides the decreased percentage of T cells in bone marrow in non-union group (31), we found that the proportion of Treg cells increased in fracture

patients compared with control individuals, and significantly decreased in non-union patients (Figure 3C). Moreover, Treg cells were clustered into two distinct populations, Treg1 and Treg2 subpopulation, as visualized by uniform manifold approximation and projection (UMAP) (Figure 3D). Interestingly, Treg2 subpopulation was barely detected in control individuals and shows much higher proportion after injury. And the frequency of Treg2 subpopulation was much lower in non-union group compared with fracture group (Figure 3D). In addition, Treg2 subpopulation exhibits high expression of genes resembling effector Treg cells (e.g. *IL2RA*, *TNFRSF4, TNFRSF18*) and preferentially expressed tissue Treg markers (e.g. *CCR8, BATF* and *GNLY*), while Treg1 subpopulation highly express transcripts (e.g. *SELL, TCF7 and LEF1*) indicative of resting phenotype (Figure 3E). GO term enrichment analysis revealed that the preponderance of biological processes related to the "regulation of stem cell differentiation," "regulation of inflammatory response," "ossification" and "wound healing" in Treg2 subpopulation (Figure 3F). Pseudotime analyses showed more terminated differentiation of Treg2 subpopulation than Treg1 subpopulation, originating from CD4 Naïve T cells (Figure 3G). Using CellPhoneDB2, a cell ligand/receptor pairing-based database (36), we identified a closer interaction and different pathway crosstalk between the Treg2 subpopulation and other cell populations in bone marrow compared with that in Treg1 subpopulation (Figure 3H, Supplemental Figure 6). Among which, CCR8-CCL1 pathway was only detected in Treg2 cluster but not in Treg1 cluster.

In summary, our data showed that bone injury induced the accumulation of a unique

"injury-responding" Treg subpopulation (Treg2) at the injury site, which was enriched with reparative signatures related to the regulation of stem cell differentiation, secreted factors, cell-cell interactions, and immunoregulation, potentially involved in bone repair.

4. Injury-responding Treg cells are marked by CCR8 and are recruited to the injury site in a CCL1-dependent way

Of note, our attention was quickly drawn to the preferentially expressed surface marker gene *CCR8* in Treg2 cluster (Figure 4A), which has been identified as the most robustly and differentially expressed chemokine receptor in tissue Treg cells (37-42). Bulk-RNA seq and ATAC-seq data also confirmed that higher mRNA expression level and more abundant chromatin accessibility of *Ccr8* in Tregs cells isolated from injury bone tissue (Figure 4B-C). Compared with $CCR8^-$ Treg cells, $CCR8^+$ Treg cells expressed much higher level of activation markers, CD44, CTLA and KLRG1. And $KLRG1^+$ $CCR8^+$ Treg cell proportion at injury site was much higher than in control bone marrow tissue (Figure 4D). Moreover, consistent with the rising tendency of total Treg cells at the injury site, the fraction of $CCR8^+$ Treg cells elevated from day 3, peaked on day 7 (51.9 ± 11.28% vs 8.3 ± 2.04% on day 0) and remained high until at least 28 days post-injury (Figure 4E-F). All these data suggested that the CCR8 marked the unique bone injury-responding Treg cells that accumulated at the injury site.

Next, we asked the origin of the accumulated $CCR8^+$ Treg cells at the injury site. In contrast to the increased proportion and number of $CCR8^+$ Treg cells at the injury site,

$CCR8^+$ Treg cells proportion and number in the adjacent inguinal lymph node was decreased after surgery (Figure 4E-G). In the spleen and peripheral blood, the proportion and the number of $CCR8^+$ Treg cells remained unchanged (Figure 4E-G). These data suggested the migration of $CCR8^+$ Treg cells from periphery to the injury site. Treatment with FTY720, an S1P receptor antagonist that inhibits lymphocytes peripheral tissue immigration (26), significantly reduced the percentage of $CCR8^+$ Treg cells at the injury site, which confirmed that peripheral $CCR8^+$ Treg cells contributed to the accumulation of $CCR8^+$ Treg cells at the injury site (Figure 5A-B).

We further investigated the mediators inducing the $CCR8^+$ Treg cells migration after injury through utilizing a quantitative reverse transcription (qRT)-PCR-based chemokine-expression array to examine the expression level of known CCR8 ligands. We observed a pronounced and highly preferential increased expression of *Ccl1* within the wound/callus tissue, which was detectable on day 3 and sustained to day 14 post-injury (Figure 5C). *In vitro* chemotaxis assay demonstrated the effect of CCL1 in recruiting $CCR8^+$ Treg cells (Figure 5D-F). Furthermore, we showed that macrophages were a major source of CCL1 in bone marrow (Figure 5G). IF staining showed that CCL1 was expressed at much higher level in macrophages at the injury site (Figure 5H). IL-6, which has been reported highly expressed in the early post-bone injury period (43, 44), significantly increased *Ccl1* gene expression in macrophages (Figure 5I). These data suggested that local production of CCL1 from macrophages was related with the early acute inflammation following bone injury.

Then a series of loss- and gain-of-function experiments were performed to evaluate the function of the CCR8/CCL1 axis in the accumulation of $CCR8^+$ Treg cells after injury (Figure 6A). CCR8 inhibitor, ML604086, demonstrating a significant effect in inhibiting CCL1 binding to CCR8 (Supplemental Figure S7), and CCL1-nuetralizing antibody (CCL1 inhibitor), were employed to interrupt the CCL1/CCR8 axis (Figure 6A, Supplemental Figure S8A).

Within the injury site, the proportions and numbers of $CCR8^+$ Treg cells and total Treg cells were significantly reduced in mice treated with CCR8 inhibitor or CCL1 inhibitor compared to untreated mice on P7. (Figure 6B-C, Supplemental Figure 8B-C). And the $CCR8^+$ Treg cells proportions and numbers in the adjacent lymph node is increased in the CCR8 inhibitor and CCL1 inhibitor treated groups (Figure 6D, Supplemental Figure 8D). These results showed that $CCR8^+$ Treg cells expanded, during the bone repair response, in a CCL1-dependent manner.

Since CCR8 inhibitor and CCL1 inhibitor treatment impaired $CCR8^+$ Treg cell accumulation at the injury site, we further explored whether bone healing was affected. We first examined the distribution of SSC lineage cells at the injury site on day 7 post-injury. The results showed that the total SSC lineage cells, SSCs, and BCSPs frequencies significantly declined in the CCR8 inhibitor/CCL1 inhibitor-treated groups (Figure 6E, Supplemental Figure 8E). Safranin O staining results indicated that the CCR8 inhibitor/CCL1 inhibitor treatment decreased cartilage formation on P14 (Figure 6F,G,

Supplemental Figure 8F). HE staining confirmed a significant impairment of defect healing in the CCR8 inhibitor/CCL1 inhibitor-treated groups on P28 (Figure 6F, Supplemental Figure 8G). Fracture model also showed prohibited bone repair in CCR8 inhibitor/CCL1 inhibitor-treated groups (Figure 6H-I, Supplemental Figure 8H-I).

Together, these findings demonstrated that $CCR8^+$ Treg cells enabled bone repair in a CCL1-dependent manner.

5. Bone injury-responding Treg cells-derived PGRN promotes SSCs osteogenic function and bone repair

In search of the underlying mechanism involved in the bone-repair role of this injury-responding Treg subpopulation, we focused on their expression of secreted factors. Several genes encoding classical trophic factors (25-30), including *Areg*, *Penk*, *Spp1*, and *Sparc*, known to promote tissue repair, did not show a significant difference between Treg-injury cells and Treg cells from the uninjured bone in our data (Figure 7A). However, gene encoding an osteogenic factor (45, 46), PGRN, were preferentially expressed in Treg-injury cells (Figure 7A) and Treg2 subpopulation (Figure 7B). ATAC-seq analysis confirmed more abundant chromatin accessibility of *Grn* in Treg cells at the injury site (Figure 7C). In addition, flow cytometry analysis showed that $CCR8^+$ Treg cells expressed much higher level of PGRN compared with $CCR8^-$ Treg cells and the expression level was further induced by injury (Figure 7D-E).

These results prompted us to explore the role of Treg-derived PGRN in mediating SSCs function and bone repair through using *Grn*$^{-/-}$ mice. *Grn* deletion did not affect the percentage of total Treg cells and CCR8^{+} Treg cells (Figure7F, I). And *Grn*$^{-/-}$ Treg cells showed similar immunosuppressive function compared with *WT* Treg cells (Supplemental Figure 9A-B). *In-vitro* multipotential differentiation assay showed that supernatant from cultured *Grn*$^{-/-}$ Treg cells displayed impaired effect in inducing SSCs osteogenic differentiation compared with the SSCs treated with *WT* Treg cells supernatant (Figure 7G-H). Furthermore, we adoptively transferred Treg cells derived from *WT* or *Grn*$^{-/-}$ mice into Treg depleted mice after bone injury (Figure 7J). The results showed that increased IFN^{+} and TNF-α^{+} Teff cells percentages induced by Treg-depletion was decreased by transferring *Grn*$^{-/-}$ Treg cells or *WT* Treg cells (Supplemental Figure 9C-D). However, *Grn*$^{-/-}$ Treg cells transferring group still showed massive fibrous tissue infiltration at the injury site without cortical fusion (Figure 7K-L, Supplemental Figure 10). While transferring of *WT* Treg cells or adding of PGRN protein resulted in better healing outcome with both callus formation and cortical fusion (Figure 7K-L, Supplemental Figure 10). These *in vivo* and *in vitro* data collectively demonstrated the importance of PGRN in mediating Treg cell-SSC crosstalk and thereby promoting bone repair.

6. BATF drives PGRN expression in the injury-responding Treg cells

We next explored the driving transcription factors that essential for repair capacity of injury-responding Treg cells in the bone injury tissue. De novo motif analysis of DNA sequences enriched under the ATAC-seq peaks showed the top significantly enriched transcription factor binding sites for genes expressed in Treg-Cntrl cells and Treg-Injury

cells, and among which, transcription factor binding sites for *Batf* was higher enriched in Treg-Injury cells (Figure 8A-C). ScRNA-seq and bulk-RNA seq also showed that gene encoding BATF was highly expressed in the Treg2 cluster and Treg-injury cells (Figure 8D, Figure 3A). Flow cytometry analysis also confirmed that $CCR8^+$ Treg cells expressed much higher level of BATF compared with $CCR8^-$ Treg cells (Figure 8E-F).

Since BATF has been widely shown to reorganize chromatin structure and differentiation of T cells (47), thus we asked whether BATF is crucial for injury-responding Treg cells repair capacity, especially for their secretion of PGRN. We first overlaid the Batf chip seq data (GSE39756) with *Grn* chromatin accessibility through ATAC-seq data and found that the *Grn*-specific binding peak on chromosome 11 maps the 5′-region of the *Batf* gene (Figure 8G). Therefore, we speculated that BATF may bind to the *Grn* promoter to activate its transcription. The JASPAR database identified the predicted *Grn* binding sites within the BATF (Figure 8H). The binding sites with highest score were located in -1788– -1778 bp, upstream of the transcription start site.

To further determine the effect of BATF-mediated *Grn* promoter activation, we mutated the BATF binding sites in the *Grn* promoter and individually transfected the respective plasmids containing either mutated or wild-type promoter regions into HEK293A cells overexpressing BATF. As expected, we found significantly increased *Grn* promoter activity induced by BATF compared with the activity of mutated *Grn* promoter (Figure 8I), which indicated that the BATF highly promoted the transcription of *Grn*.

We then examined whether CCL1 increased the BATF expression level of Treg cells when mediating the accumulation of Treg cells to the injury site. To test this, we cultured isolated Treg cells *in vitro* w/o treatment of CCL1. Flow cytometry results showed that

CCL1 treatment increased the positive percentage of BATF and also PGRN in Treg cells (Figure 8J), which suggested that CCL1 could be a potential therapeutic strategy for improving bone repair capacity of Treg cells and bone related disease.

Discussion

Upon bone injury, numerous immune cells and stromal cells accumulate within the injury site to constitute a specific local microenvironment for recruiting and activating endogenous stem cells and initiating the repair process (11). Advanced knowledge of the crucial signals that instruct skeletal stem cell function at the injury site is necessary for guiding bone repair and regeneration. Macrophages and neutrophils have been widely studied for their important roles in mediating stem cell recruitment and bone repair. Still, their accumulation is mainly in the early inflammation phase, not in the middle or late stage of the repair process (5, 12). Additional factors are necessary for switching off the inflammatory phase of wound healing and initiating the repair/regeneration process. The present study showed the indispensable and long-lasting role of Treg cells on bone repair through direct interaction with skeletal stem cells and not simply through controlling inflammation. First, we observed a significantly increased number of Treg cells in the injury niche through the whole repair process, which peaked on day seven, then remained at a high level, and slowly returned to a normal level 28 days after injury. Second, Treg cell depletion led to decreased SSCs number at the injury site by inhibiting SSCs accumulation and osteogenic differentiation, thereby generating an undersized, improperly composed callus after bone injury.

Treg cells display remarkable tissue-specificity and can exhibit distinct features in response to external stimulation (34, 35). Thus it is essential to examine whether Treg cells within the bone injury site differ from those outside the injury site in phenotype, function, and transcriptional profile, as these may help explain the mechanisms that instruct Treg cells to communicate with SSCs. Here, combined with scRNA-seq of bone marrow Treg

cells in fracture patients and bulk-RNA seq of Treg cells isolated from mouse injured femur tissue, we found that a bone injury-responding Treg population marked by CCR8 displayed a distinct tissue-repair phenotype. Compared to the $CCR8^-$ Treg cells, $CCR8^+$ Treg cells showed a higher activation level and tissue repair capacity by increased expression of CD44, CTLA, KLRG1 and BATF and enriched with bone formation pathway and stem cell regulation pathway. Interestingly, the observed phenotype presented two sets of features: one associated with stem cell regulation that has been previously reported in multiple organs and tissues and another characteristic for bone.

It is worth noting that $CCR8^+$ Treg cells also exist in the bone tissue, lymph node and spleen but in a very low proportion under normal conditions. $CCR8^+$ Treg cells number significantly increased at the injury site along with decreased number of $CCR8^+$ Treg cells in the adjacent lymph node. FTY720 treatment inhibited this change, which suggested the migration of $CCR8^+$ Treg cells from periphery to the injury site. Upon injury, the CCR8 ligand, CCL1 was highly produced from macrophages within the injury site, a response triggered by the local inflammatory cytokines. *In vivo* evidence has been procured through treatment with CCR8 inhibitor/CCL1 inhibitor, complimented by *in vitro* evidence via a chemotaxis assay, affirming the capacity of CCL1 to mobilize $CCR8^+$ Treg cells to the injury site, which indicated the pivotal role CCL1 plays in bone repair.

More importantly, these injury-associated $CCR8^+$ Treg cells secreted specific osteogenic factor, PGRN, to mediate their crosstalk with SSCs. Previously reported classical tissue repair factors such as AREG, PENK or SPP1 did not show significant increased expression in these $CCR8^+$ Treg cells. The loss-of-function of PGRN didn't affect the immunosuppressive function in Treg cells, but impaired their role in regulating SSCs'

osteogenesis function and bone healing. Our data suggested that PGRN could be a potential therapeutic target to treat bone diseases in which the patients have a lower proportion of Treg cells, such as AIDS-related fractures and osteoporosis. More importantly, a transcription factor, BATF has been demonstrated to regulate the secretion level of PGRN in the injury-responding Treg cells.

Taken together, we identified a specific bone-repair Treg subpopulation highly expressed surface marker CCR8, which infiltrated into the bone injury site in response to CCL1, directly cross-talked with SCCs through secreting PGRN to promote SSCs osteogenic function and the new bone formation. Targeting $CCR8^{+}$ Treg cells and their products could provide a potential strategy for accelerating bone healing and treating skeletal diseases.

Methods

Sex as a biological variable

Our study exclusively examined male mice to reduce female sexual cycle–related variation.

Mouse strain

All mice were maintained on a C57BL/6j background. The B6.129(Cg)-*Foxp3*^{tm3Ayr}/J (*Foxp3*-DTR mice) (48) from Jackson Laboratory were used for the pharmacological ablation of Treg cells. The human diphtheria toxin receptor expressing *Foxp3*-DTR mice was generated by integrating human DTR and enhanced green fluorescent protein (EGFP) sequences into the stop codon of the *Foxp3* gene. *Grn*$^{-/-}$ mice from Cyagen Biosciences (C57BL/6J-Grnem1C/Cya, S-KO-02346) were used for isolating *Grn* deleted Treg cells. Mouse genotypes were determined by PCR of genomic DNAs extracted from mice tails. Primer sequences were listed in Supplemental Table 2. Two-month-old male mice were used and analyzed in all experiments. Control male littermates were analyzed in all experiments. The results were expected to be relevant for both sexes. All mice were housed in specific-pathogen-free animal care facilities under a 12-h light-dark cycle with a temperature of 18–24 °C and humidity of 35–60%.

Treg ablation in *Foxp3*-DTR mice was induced by DT (5 μg/kg, Cat# D0564, Sigma-Aldrich) immediately after defect surgery or sham surgery and repeated every two days until sacrifice. To retain lymphocytes in secondary lymphoid tissue, FTY720 (Cat# SML0700, Sigma-Aldrich) was injected intraperitoneally into mice at 1 mg/kg, one day before surgery and repeated every two days until sacrifice.

Bone defect injury models

A unilateral midshaft femoral defect injury model was produced in the left femur as previously described (49). Mice were anesthetized with isoflurane gas, and a small incision was made medial to the femur tuberosity. Standardized femur injury was performed 5mm distal to the growth plate using a Micro-Drill with a 2 mm diameter stainless steel burr, and wounds were sutured. After recovery, animals were returned to housing cages. All animals received buprenorphine pre- and postoperatively for pain control.

Modified Bonnarens and Einhorn's adapted fracture method was used for the fracture study (50). Isoflurane gas was used to anesthetize mice, and buprenorphine was given to all experimental animals before surgery. After making an anterior longitudinal midline incision centered over the knee joint, a 30-gauge needle, as an intramedullary pin, was driven through the distal femur toward the femoral head after subluxation of the patella. The needle was clipped and gently nested into the distal femur to avoid soft tissue damage. A custom guillotine-style fracture device, driven by a dropped weight, was used to generate femoral fracture. The weight was determined as the amount needed, from a defined height, to generate an impact leading to a focal transverse fracture at the mid-diaphysis.

Histology and Immunohistochemistry

Femurs were collected at the indicated time points following surgery. Specimens for paraffine sections were fixed for one day in 4% paraformaldehyde in PBS at 4 ℃ and then decalcified in 15% EDTA (Cat# E1170, Solarbio). Decalcified femoral sections were stained with HE or Safranin O according to the manufacturer's protocol. TRAP activities in femur bones were tested in control mice and Treg-depleted mice, respectively, according

to the manufacturer's protocol. All bright-field images were captured on an Olympus BX-51 upright light microscope with an Olympus DP70 camera.

Immunofluorescence staining

Femur tissue was quickly harvested and embedded in optimum cutting temperature (OCT) compound (Cat# 4583, Sakura). Then, immunofluorescent staining was performed on 7 μm cryosections. Sections were blocked with 1% BSA for 60 min, permeabilized with 0.1% Triton X-100 in PBS for 15 min and then incubated with primary antibodies overnight at 4 °C. Later, the tissue sections were incubated with the appropriate fluorescent secondary antibodies for 1 h at room temperature and avoid exposure to light. Subsequently, DAPI was used to label the nuclei. Confocal microscopy (FluoView FV1000; Olympus) was used to capture images.

Micro-computed tomography (μCT) analysis

μCT scanning was performed to measure the microstructure of the bone callus. The femurs were dissected with the muscle left intact (to avoid bone callus damage), immediately fixed overnight in 4% paraformaldehyde at 4°C, and stored in 70% ethanol, until scanned by μCT (Scanco μCT-100) with an isotropic voxel size of 12 μm. μCT analysis was performed using CTAn (Bruker) in accordance with the recommendations of the American Society for Bone and Mineral Research (51). Volumes of interest (VOI) was defined by manually

outlining a region of interest encompassing the callus. All analyses were performed in a blinded fashion.

Immune cells isolation and flow cytometry

To obtain cells from the injury site, the injured femur was harvested from the hip joint to the knee joint to avoid disturbing the callus tissue. Most of the surrounding soft tissues were removed with care not to disturb the injury tissue. The top and bottom portions of the femur at approximately 2 mm above and below the injury area was excised to obtain the bone callus (including the nearby BM). The remaining tissue was cut into pieces and then transferred to a dish with 1 mL of digestion buffer containing 1 mg/ml of Collagenase D (Cat# 11088882001, Roche), 2 mg/ml of Dispase II (Cat# 10165859001, Roche) and 10000 unit/ml of DNase I (Cat# 4716728001, Roche). Callus tissue was digested for 10 minutes at 37 °C under gentle agitation and filtered through 70-μm nylon mesh to acquire single-cell suspension. Splenocytes and inguinal lymph node from the operated side were dissociated into a single-cell suspension by mechanical disruption and filtering through 70-μm nylon mesh. Venous blood was sampled in 10.0 ml Becton Dickinson (BD) Vacutainer blood collection tubes containing ethylenediamintetraacetic acid. For all samples, erythrocytes were removed with red blood cell lysis buffer (Cat# 420302, BioLegend).

For the analysis of cell surface markers, single cells were stained with indicated antibodies in PBS containing 2% FBS (Cat# 10-082-147, Gibco) at 4 ℃ in the dark. FOXP3 and other intracellular markers were stained with corresponding antibodies using the FOXP3/Transcription Factor Staining Buffer Set (Cat# 00-5523-00, eBioscience) according to the manufacturer's instructions. For PGRN staining, cells were stained with

anti-PGRN and rabbit IgG Isotype control for PGRN, respectively, followed by the incubation of APC-labeled anti-rabbit secondary antibody. To determine cytokine expression, cells were stimulated with phorbol12-myristate 13-acetate (50 ng/ml, Cat# P1585-1MG, Sigma-Aldrich), ionomycin (1μM, Cat# I3909-1ML, Sigma-Aldrich), Golgi Stop (Cat# 554724, BD Pharmingen) and Golgi Plug (Cat# 555029, BD Pharmingen) for 4 h. At the end of stimulation, cells were stained with fixable viability dye eFluor 780 and the indicated antibodies using the Intracellular Fixation and Permeabilization Buffer Set (Cat# 88-8824-00, eBioscience) following the manufacturer's instructions.

All staining was performed on ice to maintain cell morphology. Flow cytometric data were acquired using a BD FACSdiva LSR-II flow cytometer (BD Biosciences, New Jersey, USA) and analyzed using FlowJo software v10.0.6. (FlowJo LLC, Oregon, USA). Gating determinations were performed using FMO (Fluorescence Minus One) and isotype controls.

SSCs isolation and flow cytometry

Callus tissue and control limbs were dissociated by mechanical and enzymatic digestion (1 mg/ml of Collagenase P (Cat# 11213857001, Roche), 2 mg/ml of Dispase II, and 10000 units/ml of DNase I) for 1 hour at 37 °C under gentle agitation. After digestion, cells were passed through a 40 μm cell strainer and washed with staining buffer (PBS containing 2% FBS). The digested cells were subsequently blocked with BD Pharmingen™ purified rat anti-mouse CD16/CD32 antibody for 10 minutes on ice and then stained with indicated antibodies in the dark for 1 h on ice. Cells were then washed several times and resuspended in a staining buffer with DAPI (1 μg/ml, Cat# D1306, Invitrogen). The strategy to sort skeletal progenitors was diagrammed in Supplemental Figure 4. Therefore, the total SSC

lineage cells ($CD45^-Ter119^-CD31^-Thy1^-6C3^-CD51^+$), the SSC cells ($CD45^-Ter119^-CD31^-Thy1^-6C3^-CD51^+CD105^-$), the BCSP cells ($CD45^-Ter119^-CD31^-Thy1^-6C3^-CD51^+CD105^+$), and $Thy1^+$ cells ($CD45^-Ter119^-CD31^-CD51^+Thy1^+6C3^-$) were collected from the callus tissues or control limbs.

Antibodies

All antibodies used in this study are listed in Supplemental Table 1.

Generation of Treg cells in-vitro culture supernatant

Murine $CD4^+TCR\beta^+CD25^{high}GFP^+$ Treg cells were sorted from spleen and lymphoid tissue and stimulated with anti-CD3/CD28 DynaBeads (one cell to one bead, Cat# 11453D, Invitrogen) in the presence of mIL-2 (50 U/ml, Cat# 402-ML, R&D) for 24 h. Anti-CD3/CD28 DynaBeads were further removed from the culture. Mouse Treg cells were cultured in RPMI 1640 medium (plus β-mercaptoethanol, Cat# M7522, Sigma-Aldrich) supplemented with 10% FBS, 1% GlutaMax (Cat# 11360070, Gibco), 1% sodium pyruvate (Cat# 11360070, Gibco) and 1% pen/strep (Cat# 1507006, Gibco). The culture medium was changed every 2-3 days, followed by the re-supplementation of cytokines. After four days, the supernatant was collected and stored at -80 °C.

To investigate the function of PGRN, $CD4^+TCR\beta^+CD25^{high}$ Treg cells were isolated from *Grn*$^{-/-}$ mice and cultured *in vitro* as previously described. After four days, the supernatants were collected and stored at -80 °C.

SSCs culture with Treg cells culture supernatant and multiple differentiation assay

Sorted SSCs were cultured in MEM-α medium (Cat# 12561056, GIBCO), containing 10% FBS and 1% penicillin/streptomycin, for one week. Then SSCs at passage 1 were plated in a single well of a 6-well plate at the density of 1×10^4 cells/ml for 12 h. To induce osteoblast differentiation, cells were cultured with a complete culture medium supplemented with 1 μM dexamethasone (Cat# D4902, Sigma-Aldrich), 10 mM β-glycerophosphate (Cat# G9422, Sigma-Aldrich), and 50 μg/ml ascorbic acid (Cat# A5960, Sigma-Aldrich) for 14 days. Treg culture supernatant was diluted to 1:5 and added to SSCs culture medium. The culture medium was replaced every 3 days for up to 2 weeks. Cells were then fixed with 4% paraformaldehyde for 15 min and stained with the BCIP/NBT ALP Staining Kit (Cat# C3206, Beyotime) following the manufacturer's instructions. To induce adipocyte differentiation, cells were cultured with a full culture medium containing 1 μM dexamethasone (Cat# D4902, Sigma-Aldrich), 0.5 mM IBMX (3-Isobutyl-1-methylxanthine, Cat# I5879, Sigma-Aldrich) and 1 μg/ml insulin (Cat# I6634, Sigma-Aldrich). Culture media were exchanged with fresh media every 3–4 days for up to 2 weeks. Treg culture supernatant was diluted to 1:5 and added to SSCs culture medium. Cells were then fixed with 4% paraformaldehyde for 15 minutes and stained with 0.3% Oil Red O solution (Cat# O0625, Sigma-Aldrich).

RNA preparation, qRT-PCR, and bulk RNA-Seq

Total RNA from the isolated callus tissue was extracted using Trizol reagent (Cat# 15596018, Invitrogen) following the manufacturer's instructions, and was reverse-transcribed into cDNA with iScript cDNA Synthesis Kit (Cat# 170-8890, Bio-Rad). qRT-

PCR was performed with TB Green Premix Ex Taq II kit (Cat# RR82WR, TaKaRa) with primers listed in Supplemental Table 2.

For SSCs and Treg cells bulk RNA-Seq analysis, one thousand fresh SSCs or Treg cells from callus tissue of Treg-depleted mice and control mice 7 days after surgery and from bone marrow tissue at steady state were collected by FACS. Total RNA was then extracted for generating sequencing libraries by using the TruSeq RNA Sample Prep Kit (Cat# RS-122-2001, Illumina). The barcoded samples were pooled and then sequenced on an Illumina Hiseq platform, and 125 bp/150 bp paired-end reads were generated. The RNA-seq library generation and sequencing were performed at Novogene Corporation. Heatmap was used to display relative transcript levels of genes of interest by using normalized FPKM values from Cuffnorm. Volcano plot was generated by ggplot2 package in R. The pathway gene sets used in this work were extracted from the online databases Kyoto Encyclopedia of Genes and Genomes (KEGG), Gene Ontology, BioCarta, Reactome and curated Hallmark gene sets. Function terms or pathways were considered significant if Benjamini–Hochberg adjusted FDR<0.05.

Bioinformatics analysis of single-cell RNA sequencing data

For analysis of scRNA-seq data from bone marrow of human patients with fracture, fracture nonunion and from normal bone marrow, raw FASTQ data was derived from PRJNA900553 and then was extracted into a Seurat object. Quality control was processed by filtering out these cells: 1) gene numbers less than 200, UMI less than 1000

and log10GenesPerUMI less than 0.7; 2) >10% of the counts belonged to mitochondrial genes and >5% of the counts belonged to hemoglobin genes. Quality control revealed no significant batch effect, and similar distributions were observed for the metrics mentioned above across different runs and experiments. Detailed procedures are described in Supplemental Methods.

ATAC-seq and analysis

ATAC-seq was performed according to the Omni-ATAC protocol (52) without modifications. A preamplification of transposed nuclear fragments was performed using primers with Illumina adaptors. Barcoded sample libraries were pooled for a final concentration of 4 nM. For sequencing data analysis, the adapters were trimmed and aligned to mm10 reference genome by Bowtie2. Reads mapped to mitochondrial DNA, with duplication or unknown identities were eliminated by Sambamba. The read depth was 80 to 90 million reads for each sample. The total number of mapped reads in each sample was normalized to one million mapped reads. Peak calling was performed using MACS285 with a q value cutoff of 0.01. The peaks were assigned to each gene locus, including 20 kb upstream of the transcription start site, gene body and 5 kb downstream of transcription termination site. For visualizing the ATAC seq data, bigwig files were created from bam files with deeptools, normalized using the Counts Per Million mapped reads (CPM) method (53), and then the peaks were visualized in Integrative Genomics Viewer (IGV). SitePro (v1.0.2) was used to visualize the average signals of ATAC-seq in

the desired genomic regions. Homer findMotifsGenome.pl (v4.8.3, homer de novo Results) was used to identify transcription factor motifs enriched at peaks.

CCL1, CCR8 inhibitor, CCL1 inhibitor treatment

For CCL1 administration *in vivo*, recombinant mouse CCL1 protein (50 μg/kg, Cat# 845-TC, R&D) in 50 μL of LPS-free PBS was injected intraperitoneally after defect surgery and repeated every three days until sacrifice. To interrupt CCL1-CCR8 axis, CCR8 inhibitor (1 mg/kg, Cat# ML604086, MedChemExpress) or CCL1 inhibitor (75 μg each, Cat# AF845, R&D) was administered intraperitoneally after defect surgery and repeated every three days (for CCR8 inhibitor) or 7 days (for CCL1 inhibitor) until sacrifice. The mice in the control group were treated with an identical volume of corn oil. For monitoring the role of CCL1 in regulating the activity of BATF and PGRN secretion in Treg cells, Treg cells were sorted from spleen and lymph node and cultured as above described. CCL1 (10 ng/ml, 50 ng/ml) was added to the culture medium after 2 hours-culture. After 24 hours, cells were collected for flow cytometry analysis.

Treg cells transfection

For Treg cells transfer experiments, Treg cells were freshly isolated from spleens of 8- to 10-week-old male *WT* and *Grn*$^{-/-}$ mice using EasySep™ Mouse CD4^{+}CD25^{+} Regulatory T Cell Isolation Kit II (Cat# 18783, STEMCELL Technologies) as above. The isolation was performed in a two-step procedure with a negative selection on CD4^{+} cells and a positive selection on CD25^{+} cells according to the manufacturer's instructions. DT treatment was given every two days after surgery. Then, 2-3 × 10^{6} Tregs diluted in 50 μL sterile PBS

were injected into recipient *Foxp3*-DTR mice 3 days after DT treatment through the lateral tail vein and repeated every 7 days. Control mice received an equivalent volume of phosphate-buffered saline (PBS). For PGRN treatment, recombinant mouse PGRN protein (50 μg/kg, Cat# HY-P74617, MedChemExpress) was administered intraperitoneally after defect surgery and repeated every three days until sacrifice.

Dual luciferase assay

Transfection for dual-luciferase reporter plasmids was performed as described above. Luciferase activity was measured using the Dual Luciferase Reporter Assay System (Cat# E1910, Promega) according to the manufacturer's instructions. In brief, HEK293A cells were transfected with the indicated plasmids using Lipofectamine 2000 (Cat# 11668027, Thermo Fisher Scientific). At 48 h after transfection, cells were lysed by passive lysis buffer and harvested the lysate. The firefly and renilla luciferase activity in the lysate were detected in triplicate using a dual-luciferase reporter assay system (Promega) according to the manufacturer's protocol and quantified using GloMax 20/20luminometer (Promega). The luciferase activity of firefly was normalized to renilla luciferase activity to determine the target gene promoter activity. Luciferase activity of promoter was expressed as fold changes of control group.

In vitro suppression assay

Teff cells ($CD4^+CD25^-GFP^-$ cells) were sorted and labeled with CellTrace Violet Cell

Proliferation dye (Cat# C34557, Thermofisher Scientific) according to the manufacturer's instructions and were used as responder cells. Then labeled Teff cells (1×10^5) were sorted and co-cultured with *Grn*$^{-/-}$ or *WT* Treg cells in the presence of 1 μg/ml soluble anti-CD3/CD28 in 96-well U-bottom plates. The ratios of Treg cells to Teff cells were 0:1, 1:1, 1:2, 1:4, 1:8 or 1:16. After 72-hour incubation, the proliferation of Teff cells was determined by flow cytometry as previously reported (54).

Statistics

Statistical analyses were performed using GraphPad Prism 6.0 (San Diego, CA, United States) with unpaired, two-sided Student's t-test for two-group comparisons. One-way ANOVA or two-way ANOVA with Bonferroni multiple comparisons test was used for multiple groups. All data are shown as mean± s.e.m. The numbers of experimental repeats are shown in figure legends. A P value of less than 0.05 was considered to be significant. *P ≤ 0.05, **P ≤ 0.01, ***P ≤ 0.005, ****P ≤ 0.001.

Study approval.

All mouse experiments complied with all relevant ethical regulations and were performed according to protocols approved by the Institutional Animal Care and Use Committees at the Shanghai Jiao Tong University and in compliance with the ARRIVE 2.0 guideline (55).

Data availability

RNA-Sequencing data and ATAC-sequencing data have been deposited in the Sequence

Read Archive under accession no. PRJNA863720, PRJNA863747. Published human sc-RNA seq dataset used in this study is accessible at the GEO under accession number: PRJNA900553. The Batf Chip seq data is accessible at the GEO under accession number: GSE39756. The binding sites of BATF within the *Grn* promoter were predicted using The JASPAR database [https://jaspar.genereg.net/]. The paper and the Supplementary Material present all data needed to evaluate the conclusions. Source data are reported in the Supporting Data Values. Other data generated or analyzed during this study are available from the corresponding authors upon reasonable request.

Author contributions: J.Y.S., H.C.L., and R.Y.C. conceived the project. R.Y.C. provided the methodology. R.Y.C., X.M.Z., Y.J.Y, Y.L., B.L.L., S.J.Q., and Y.X.G. carried out the investigations. H.C., B.L., Q.W.W., K.R.M., J.Y.S. and H.C.L. provided the resources. R.Y.C., X.M.Z., and H.C. carried out the formal analysis. X.M.Z. and H.C. curated the data. J.Y.S. and H.C.L. supervised the project. R.Y.C. and J.Y.S. wrote the original draft of the paper. M.S.T, J.Y.S., and H.C.L. edited and revised the paper. R.Y.C is listed as the first author in recognition of her significant contribution to the inception of this study.

Acknowledgments: This work was supported by the National Natural Science Foundation of China (NSFC) (82171005, 82201093), the Shanghai Rising Star Program (22QA1405200) and Shanghai Pujiang Program (22PJ1409100). We thank the support from the FACS Core Facility of Basic Medical Sciences and the sequencing core at the Shanghai Institute of Immunology, Shanghai Jiao Tong University School of Medicine. We thank R. Feng (Shanghai Jiao Tong University) for assistance in RNA-seq experiments, H. Dong (Harvard University, MA), and M.R. Wu (Zhejiang University) for helpful discussion.

References

1. Global, regional, and national burden of bone fractures in 204 countries and territories, 1990-2019: a systematic analysis from the Global Burden of Disease Study 2019. *Lancet Healthy Longev.* 2021;2(9):e580-e92.
2. Panteli M, et al. Biological and molecular profile of fracture non-union tissue: A systematic review and an update on current insights. *J Cell Mol Med.* 2022;26(3):601-23.
3. Ono N, et al. Bone repair and stem cells. *Curr Opin Genet Dev.* 2016;40:103-7.
4. Böhm A-M, et al. Activation of Skeletal Stem and Progenitor Cells for Bone Regeneration Is Driven by PDGFRβ Signaling. *Dev Cell.* 2019;51(2).
5. Pajarinen J, et al. Mesenchymal stem cell-macrophage crosstalk and bone healing. *Biomaterials.* 2019;196:80-9.
6. Sorkin M, et al. Regulation of heterotopic ossification by monocytes in a mouse model of aberrant wound healing. *Nat Commun.* 2020;11(1):722.
7. Embree MC, et al. Exploiting endogenous fibrocartilage stem cells to regenerate cartilage and repair joint injury. *Nat Commun.* 2016;7:13073.
8. Chan CKF, et al. Identification and specification of the mouse skeletal stem cell. *Cell.* 2015;160(1-2):285-98.
9. Gulati GS, et al. Isolation and functional assessment of mouse skeletal stem cell lineage. *Nat Protoc.* 2018;13(6):1294-309.
10. Okamoto K, et al. Osteoimmunology: The Conceptual Framework Unifying the Immune and Skeletal Systems. *Physiol Rev.* 2017;97(4):1295-349.
11. Ono T, et al. Osteoimmunology in Bone Fracture Healing. *Curr Osteoporos Rep.* 2017;15(4):367-75.
12. Cai B, et al. N2-Polarized Neutrophils Guide Bone Mesenchymal Stem Cell Recruitment and Initiate Bone Regeneration: A Missing Piece of the Bone Regeneration Puzzle. *Adv Sci (Weinh).* 2021;8(19):e2100584.
13. Batoon L, et al. CD169+ macrophages are critical for osteoblast maintenance and promote intramembranous and endochondral ossification during bone repair. *Biomaterials.* 2019;196:51-66.
14. Camacho V, et al. Bone marrow Tregs mediate stromal cell function and support hematopoiesis via IL-10. *JCI Insight.* 2020;5(22).
15. Liu Z, et al. Nanofibrous Spongy Microspheres To Distinctly Release miRNA and Growth Factors To Enrich Regulatory T Cells and Rescue Periodontal Bone Loss. *ACS Nano.* 2018;12(10):9785-99.
16. Kelchtermans H, et al. Activated CD4+CD25+ regulatory T cells inhibit osteoclastogenesis and collagen-induced arthritis. *Ann Rheum Dis.* 2009;68(5):744-50.
17. Sun G, et al. Regulatory B cell is critical in bone union process through suppressing proinflammatory cytokines and stimulating Foxp3 in Treg cells. *Clin Exp Pharmacol Physiol.* 2017;44(4):455-62.
18. Sun G, et al. STAT3 promotes bone fracture healing by enhancing the FOXP3 expression and the suppressive function of regulatory T cells. *APMIS.* 2017;125(8):752-60.
19. Shiau S, et al. Incident fractures in HIV-infected individuals: a systematic review and meta-analysis.

AIDS. 2013;27(12):1949-57.

20. Dong HV, et al. Osteoporosis and fractures in HIV/hepatitis C virus coinfection: a systematic review and meta-analysis. *AIDS.* 2014;28(14):2119-31.
21. Li J-Y, et al. Parathyroid hormone-dependent bone formation requires butyrate production by intestinal microbiota. *J Clin Invest.* 2020;130(4):1767-81.
22. Yu M, et al. Regulatory T cells are expanded by Teriparatide treatment in humans and mediate intermittent PTH-induced bone anabolism in mice. *EMBO Rep.* 2018;19(1):156-71.
23. Wen T, et al. Single-cell RNA sequencing identifies inflammatory tissue T cells in eosinophilic esophagitis. *J Clin Invest.* 2019;129(5):2014-28.
24. Liu Z, et al. Glucocorticoid signaling and regulatory T cells cooperate to maintain the hair-follicle stem-cell niche. *Nat Immunol.* 2022;23(7):1086-97.
25. Harb H, et al. Notch4 signaling limits regulatory T-cell-mediated tissue repair and promotes severe lung inflammation in viral infections. *Immunity.* 2021;54(6).
26. Xia N, et al. A Unique Population of Regulatory T Cells in Heart Potentiates Cardiac Protection From Myocardial Infarction. *Circulation.* 2020;142(20):1956-73.
27. Mallat Z. Regulating heart repair with cardiac-specific T lymphocytes. *J Clin Invest.* 2019;129(11):4587-9.
28. Kuswanto W, et al. Poor Repair of Skeletal Muscle in Aging Mice Reflects a Defect in Local, Interleukin-33-Dependent Accumulation of Regulatory T Cells. *Immunity.* 2016;44(2):355-67.
29. Whibley N, et al. Regulatory T cell adaptation in the intestine and skin. *Nat Immunol.* 2019;20(4):386-96.
30. Ito M, et al. Brain regulatory T cells suppress astrogliosis and potentiate neurological recovery. *Nature.* 2019;565(7738):246-50.
31. Avin KG, et al. Single-cell RNAseq provides insight into altered immune cell populations in human fracture nonunions. *J Orthop Res.* 2023;41(5):1060-9.
32. Lee S-Y, et al. A novel cytokine consisting of the p40 and EBI3 subunits suppresses experimental autoimmune arthritis via reciprocal regulation of Th17 and Treg cells. *Cell Mol Immunol.* 2022;19(1):79-91.
33. Henderson LA, et al. Next-Generation Sequencing Reveals Restriction and Clonotypic Expansion of Treg Cells in Juvenile Idiopathic Arthritis. *Arthritis Rheumatol.* 2016;68(7):1758-68.
34. Panduro M, et al. Tissue Tregs. *Annu Rev Immunol.* 2016;34:609-33.
35. DiSpirito JR, et al. Molecular diversification of regulatory T cells in nonlymphoid tissues. *Sci Immunol.* 2018;3(27).
36. Efremova M, et al. CellPhoneDB: inferring cell-cell communication from combined expression of multi-subunit ligand-receptor complexes. *Nat Protoc.* 2020;15(4):1484-506.
37. Barsheshet Y, et al. CCR8+FOXp3+ Treg cells as master drivers of immune regulation. *Proc Natl Acad Sci U S A.* 2017;114(23):6086-91.
38. De Simone M, et al. Transcriptional Landscape of Human Tissue Lymphocytes Unveils Uniqueness of Tumor-Infiltrating T Regulatory Cells. *Immunity.* 2016;45(5):1135-47.
39. Delacher M, et al. Single-cell chromatin accessibility landscape identifies tissue repair program in human regulatory T cells. *Immunity.* 2021;54(4).

40. Coghill JM, et al. CC chemokine receptor 8 potentiates donor Treg survival and is critical for the prevention of murine graft-versus-host disease. *Blood.* 2013;122(5):825-36.
41. Vila-Caballer M, et al. Disruption of the CCL1-CCR8 axis inhibits vascular Treg recruitment and function and promotes atherosclerosis in mice. *J Mol Cell Cardiol.* 2019;132:154-63.
42. Campbell C, et al. Roles of Regulatory T Cells in Tissue Pathophysiology and Metabolism. *Cell Metab.* 2020;31(1):18-25.
43. Li W-W, et al. IL-6 signaling mediates the germinal center response, IgM production and nociceptive sensitization in male mice after tibia fracture. *Brain Behav Immun.* 2021;94:148-58.
44. Furman BD, et al. Articular ankle fracture results in increased synovitis, synovial macrophage infiltration, and synovial fluid concentrations of inflammatory cytokines and chemokines. *Arthritis Rheumatol.* 2015;67(5):1234-9.
45. Wei J, et al. The role of progranulin in arthritis. *Ann N Y Acad Sci.* 2016;1383(1).
46. Zhao Y-p, et al. The promotion of bone healing by progranulin, a downstream molecule of BMP-2, through interacting with TNF/TNFR signaling. *Biomaterials.* 2013;34(27):6412-21.
47. Pham D, et al. Batf stabilizes Th17 cell development via impaired Stat5 recruitment of Ets1-Runx1 complexes. *EMBO J.* 2023;42(8):e109803.
48. Kim JM, et al. Regulatory T cells prevent catastrophic autoimmunity throughout the lifespan of mice. *Nat Immunol.* 2007;8(2):191-7.
49. Matsushita Y, et al. A Wnt-mediated transformation of the bone marrow stromal cell identity orchestrates skeletal regeneration. *Nat Commun.* 2020;11(1):332.
50. Bonnarens F, et al. Production of a standard closed fracture in laboratory animal bone. *J Orthop Res.* 1984;2(1).
51. Bouxsein ML, et al. Guidelines for assessment of bone microstructure in rodents using micro-computed tomography. *J Bone Miner Res.* 2010;25(7):1468-86.
52. Corces MR, et al. An improved ATAC-seq protocol reduces background and enables interrogation of frozen tissues. *Nat Methods.* 2017;14(10):959-62.
53. Buenrostro JD, et al. Transposition of native chromatin for fast and sensitive epigenomic profiling of open chromatin, DNA-binding proteins and nucleosome position. *Nat Methods.* 2013;10(12):1213-8.
54. Akimova T, et al. Standardization, Evaluation, and Area-Under-Curve Analysis of Human and Murine Treg Suppressive Function. *Methods Mol Biol.* 2016;1371:43-78.
55. Percie du Sert N, et al. The ARRIVE guidelines 2.0: Updated guidelines for reporting animal research. *PLoS Biol.* 2020;18(7):e3000410.

Figures

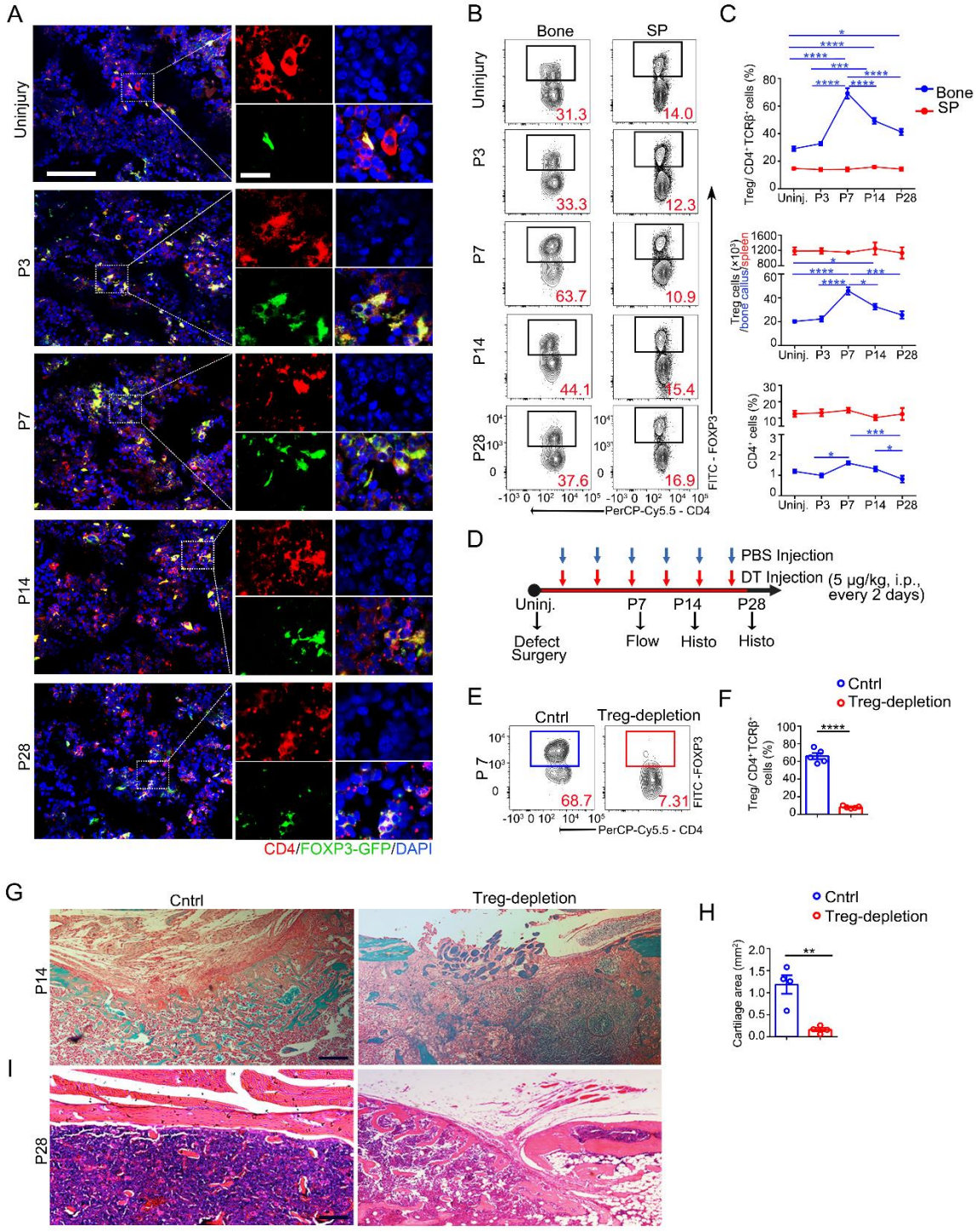

Figure 1. Treg cells accumulation in the injured bone tissue enables bone repair

(A) Representative images of co-localization of CD4 (red) and FOXP3-GFP (green) in

uninjured/injured bone tissue on day 0 (Uninjury), day 3, day 7, day 14, and day 28 post-operation. Scale bars: 100μm (Left); 10 μm (Right).

(B) Representative flow cytometry analysis of Treg cells from callus tissue on day 0 (Uninjury), day 3, day 7, day 14, and day 28 post-operation. The numbers indicate the proportion of Treg cells in the frame.

(C) The proportions of Treg cells among $CD4^+TCR\beta^+$ cells, the numbers of Treg cells, and the proportions of $CD4^+$ cells at indicated time points in bone callus tissue (Blue) and in spleen (Red). n = 4-5 per group.

(D) Diagram illustration of Treg cells depletion by DT injection after bone defect surgery.

(E) Representative flow cytometry graphs of Treg cell proportions in control group (Cntrl) and Treg-depletion group (Treg-depletion). The numbers indicate the proportion of Treg cells in the frame.

(F) The proportions of Treg cells among $CD4^+TCR\beta^+$ cells. n = 5 per group.

(G) Safranin O staining of injured bone tissues from the Control group and Treg-depletion group. Scale bars: 200μm (Left); 50 μm (Right).

(H) The Safranin O images were analyzed using Image J Ver.1.48. n = 4 per group.

(I) HE staining of injured bone tissues from the Control group and Treg-depletion group.

All data are represented as mean ± s.e.m. *$P \leq 0.05$, **$P \leq 0.01$, ***$P \leq 0.005$, ****$P \leq 0.001$, as determined by unpaired two-tailed Student's t-test (G, I) or one-way ANOVA with Bonferroni multiple comparisons test (D).

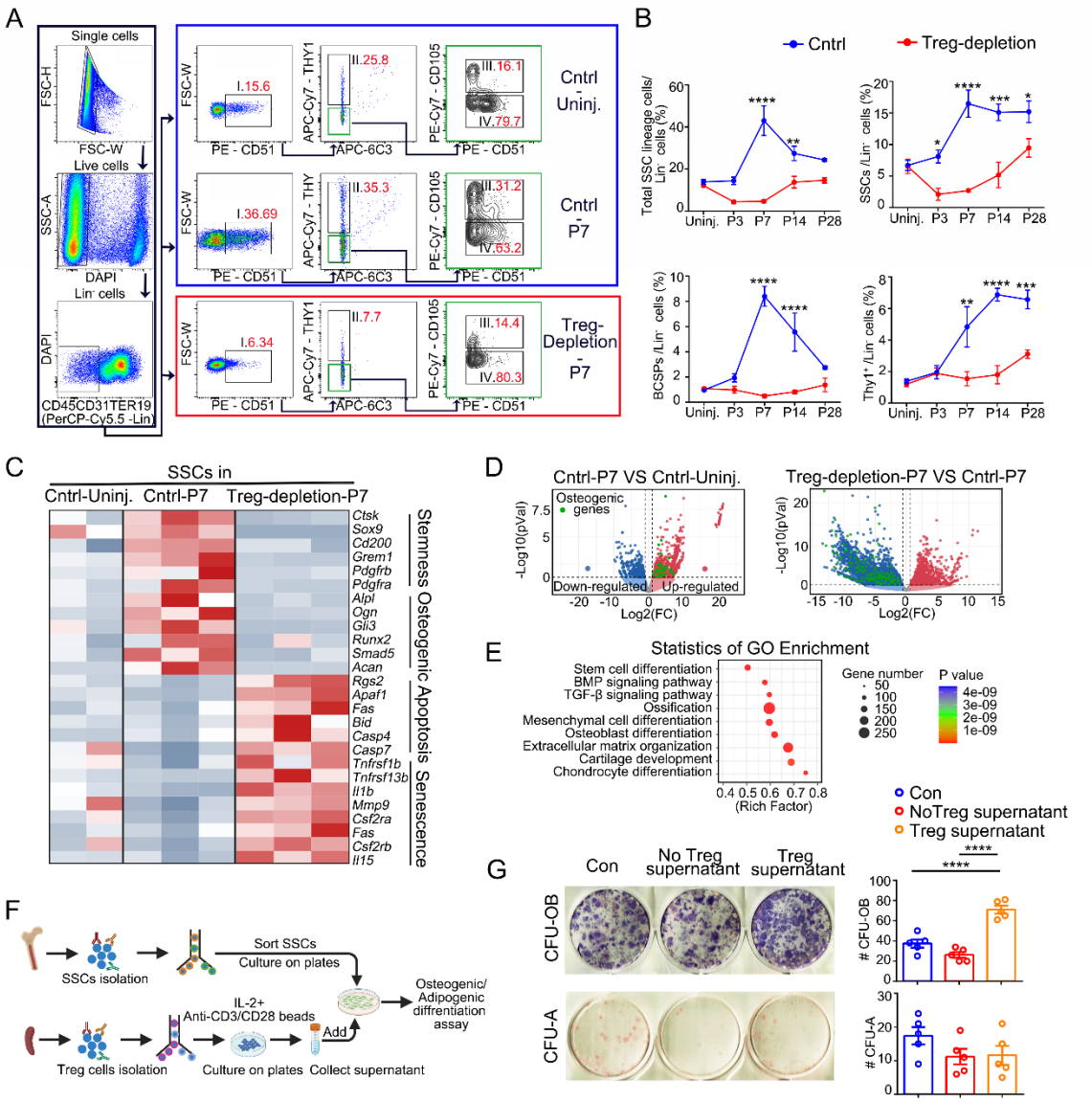

Figure 2. Treg cells promote SSCs accumulation and osteogenic differentiation.

(A) Representative flow cytometry analysis images of SSC lineage cells.

(B) The percentages of total SSC lineage cells, SSCs, BCSPs, and Thy1^{+} cells within total Lin^{-} cells from control and Treg-depletion groups at indicated time points. n = 4 per group.

(C) Heatmap of a selected list of differentially expressed transcripts among SSCs isolated 7 days after injury (Cntrl-P7), SSCs before injury (Cntrl-Uninj.) and SSCs from Treg-

depletion group 7 days after injury (Treg-depletion-P7). n = 2-3 per group.

(D) Volcano plots representation of a comparison of gene expression profiles between SSCs from Cntrl-P7 group and Cntrl-Uninj. group or SSCs from Treg-depletion-P7 group and Cntrl-P7 group. Green dots show osteogenic genes.

(E) Go analysis revealing gene ontology enrichment of the biological processes enriched in SSCs from Cntrl-P7 group compared with SSCs from Treg-depletion-P7 group.

(F) Diagram of the experimental protocol showing the isolation of Treg cells from the spleen and SSCs from the bone tissue of the same mice. The SSCs were cultured with the Treg-conditioned medium and subjected to osteogenic/adipogenic differentiation assays.

(G) Quantification of colonies of osteogenic (CFU-OB) and adipogenic (CFU-Adipo) assays showing the differentiation results of control group (SSCs cultured without adding Treg culture medium), no Treg supernatant group (SSCs cultured with adding fresh Treg culture medium) and Treg supernatant group (SSCs cultured with adding supernatant collected from cultured Treg cells dishes). n = 5 per group.

All data are represented as mean ± s.e.m. *P ≤ 0.05, **P ≤ 0.01, ***P ≤ 0.005, ****P ≤ 0.001, as determined by two-way ANOVA with Bonferroni multiple comparisons test (B) or one-way ANOVA with Bonferroni multiple comparisons test (G).

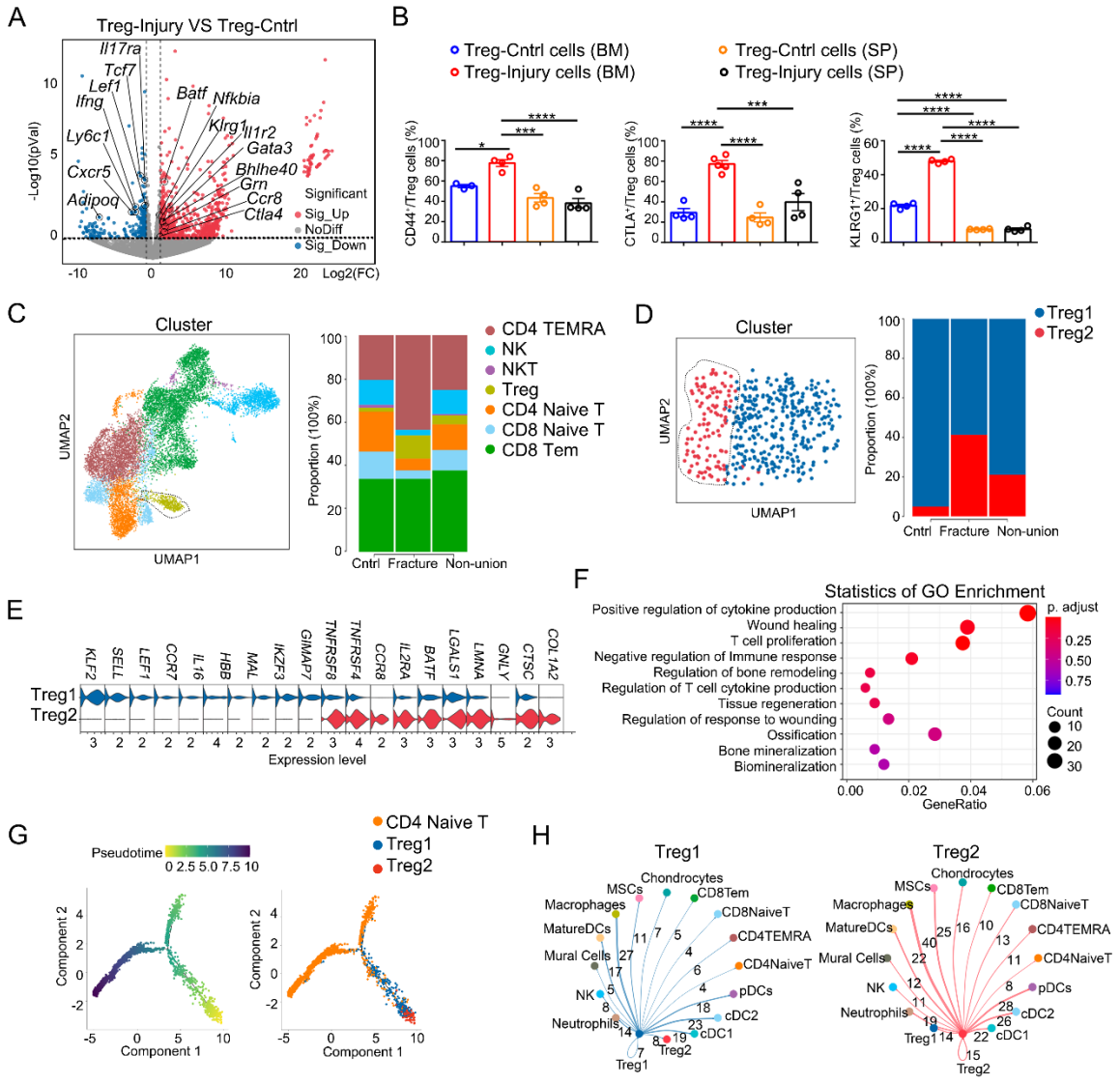

Figure 3. The distinct transcriptome of "injury-responding" Treg cells within the injury site.

(A) Volcano plots represent differentially expressed genes between Treg-Cntrl cells and Treg-Injury cells. n = 3 per group.

(B) The experiments compare the percentage of CD44, CTLA and KLRG1 positive Treg cells from the uninjured bone (blue), Treg cells from the wound/callus tissue at the injury site (red), Treg cells from the spleen of uninjured mice (orange), and injured mice (grey). n = 3-5 per group.

(C) Umap plot showing clusters and cluster annotations of bone marrow T and NK cell (Left panel). Stacked bar graph showing percentages of cells in each cluster among total NK and T lymphocytes (Right panel).

(D) Uamp plot showing clusters and cluster annotations of bone marrow Treg cells (Left panel) and stacked bar graph showing percentages of cells in each cluster among total Treg cells (Right panel).

(E) Violin plot showing the top markers for Treg1 and Treg2 subpopulation.

(F) Gene ontology enrichment of the biological process categories in Treg2 subpopulation compared with Treg1 subpopulation.

(G) Pseudotime analyses showing the differentiation of Treg1 subpopulation and Tre2 subpopulation from CD4 Naïve T cells.

(H) Network diagram of the interaction between Treg1 (right panel) or Treg 2 (left panel) cluster and other cells in the bone marrow. The size of the circle represented the number of interactions with all other types of cells, and the thickness of the line represented the interaction number of cells between the line.

All data are shown as mean ± s.e.m. *P ≤ 0.05, ***P ≤ 0.005, ****P ≤ 0.001, as determined by one-way ANOVA with Bonferroni multiple comparisons test.

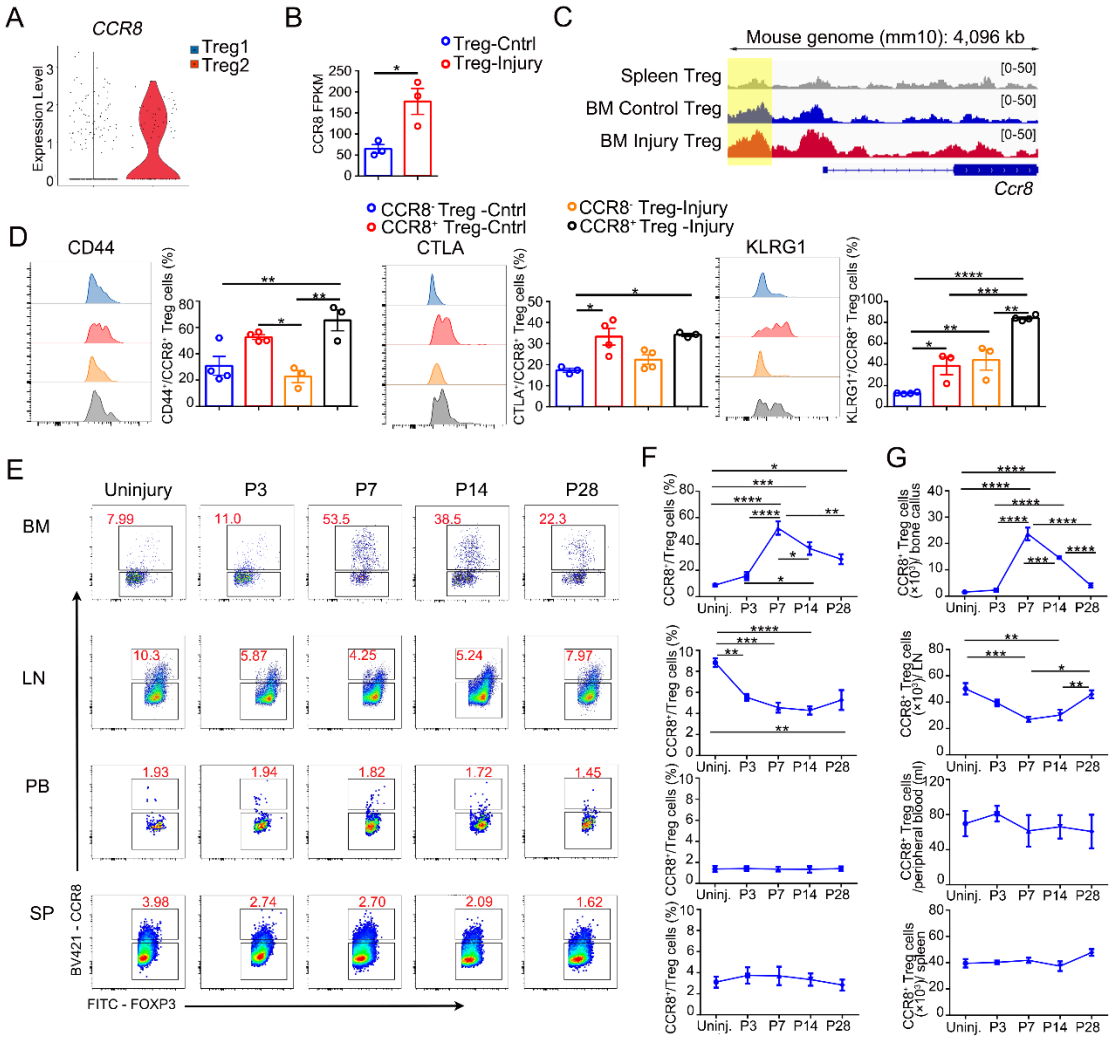

Figure 4. Bone injury-responding Treg population accumulate at the injury site marked by CCR8 and migrate from periphery

(A) Violin plots of *CCR8* gene expression in Treg1 subset and Treg2 subset.

(B) Statistical analysis of *Ccr8* gene expression in Treg cells from uninjured bone and injured bone. n = 3 per group.

(C) Chromatin accessibility of the *Ccr8* locus in spleen Treg cells, bone marrow Treg cells in control and injury group.

(D) Representative histograms (left pannel) and statistical analysis (right pannel) of the

expression of CD44, GTLA and KLRG1 in $CCR8^{+/-}$ Treg cells from different sources: uninjured bone (blue for $CCR8^{-}$ and red for $CCR8^{+}$) and injury site (orange for $CCR8^{+}$ and black for $CCR8^{-}$). n = 3-4 per group.

(E) Representative flow images of the proportions of $CCR8^{+}$ Treg cells among total Treg cells in bone marrow (BM), adjacent inguinal lymph node (LN), peripheral blood (PB) and spleen (SP) before surgery and 3, 7,14, and 28 days after surgery.

(F) Statistical analysis of the proportions of $CCR8^{+}$ Treg cells among total Treg cells in BM, LN, PB and SP at indicated time points. n = 4-5 per group.

(G) The numbers of $CCR8^{+}$ Treg cells in BM, LN, PB and SP at indicated time points. n = 4-5 per group.

All data are shown as mean ±s.e.m. *$P \leq 0.05$, **$P \leq 0.01$, ***$P \leq 0.005$, ****$P \leq 0.001$, as determined by unpaired two-tailed Student's t-test (B), one-way ANOVA with Bonferroni multiple comparisons test (D, F, G).

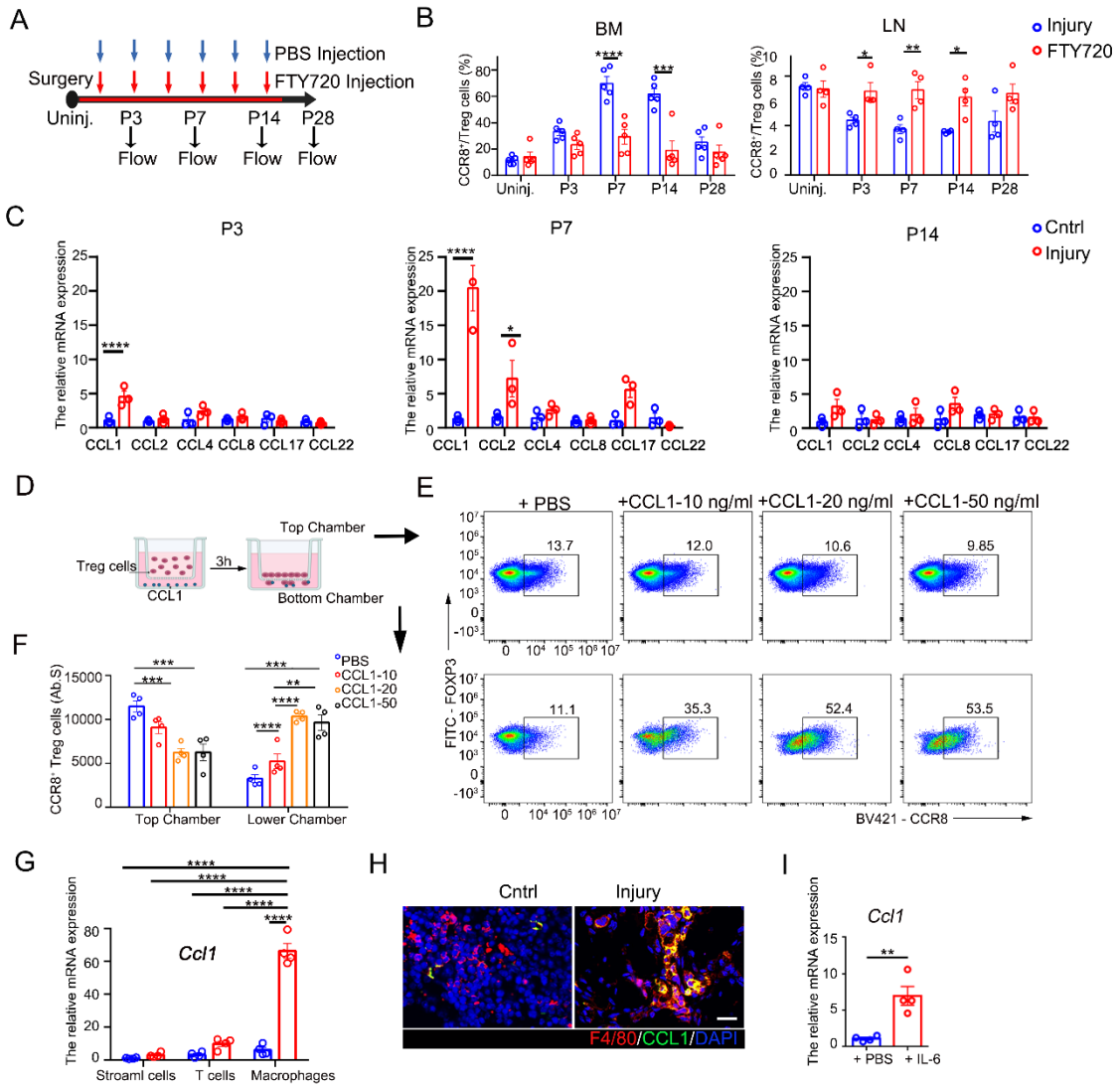

Figure 5. Macrophages derived CCL1 mediated CCR8$^+$ Treg cells migration into the injury site

(A) Schematic diagram showing the FTY720 treatment protocol.

(B) The fractions of CCR8$^+$ Treg cells among total Treg cells in the control group (Cntrl) and FTY720 treated group (FTY720-Treated) in bone marrow and adjacent lymph node at indicated time points. n = 4-5 per group.

(C) Transcript levels of chemokine ligand gene transcripts in the wound/callus tissue and control tissue were quantified by qRT-PCR before surgery and on days 3, 7, and 14

after injury. n = 3 per group.

(D) Schematic diagram showing CCL1 mediated chemotaxis assay protocol.

(E) Representative flow images of the proportions of $CCR8^+$ Treg cells among total Treg cells in top/bottom chambers treated with CCL1 at indicated concentrations.

(F) The number of $CCR8^+$ Treg cells in top/bottom chambers treated with CCL1 at indicated concentrations. n = 4 per group.

(G) The relative expression level of *Ccl1* in stromal cells, T cells and macrophages derived from bone marrow tissue in control and bone injury mice. n = 4 per group.

(H) Representative images of co-localization of F4/80 (red) and CCL1 (green) in control/injured bone tissue. Scale bars: 10 μm.

(I) The relative expression level of *Ccl1* in bone marrow macrophages treated with PBS or IL-6. n = 4 per group.

All data are shown as mean ±s.e.m. *P ≤ 0.05, **P ≤ 0.01, ***P ≤ 0.005, ****P ≤ 0.001, as determined by two-way ANOVA with Bonferroni multiple comparisons test (B, C, F) or one-way ANOVA with Bonferroni multiple comparisons test (G) or unpaired two-tailed Student's t-test (I).

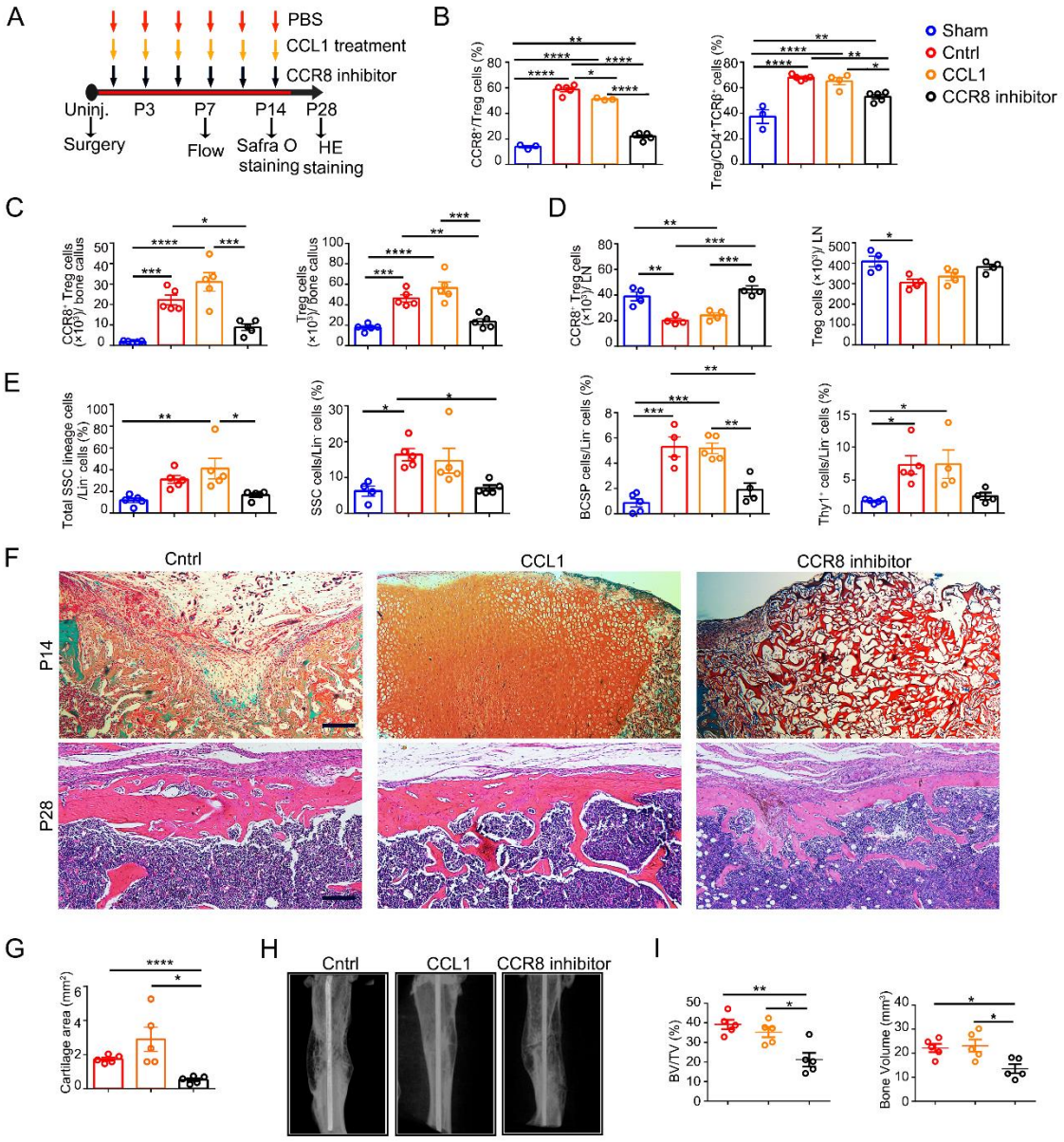

Figure 6. CCR8$^+$ Treg cells promote bone repair in a CCL1-dependent manner.

(A) Schematic diagram showing the CCL1 and CCR8 inhibitor treatment protocol.

(B) Proportions of CCR8$^+$ Treg cells among Treg cells and Treg cells among CD4$^+$ TCRβ$^+$ cells from uninjured group (Sham, blue) and from injury site at control group (Cntrl, red), CCL1 treated group (CCL1, yellow) and CCR8 inhibitor treated group (CCR8 inhibitor, black) on seven days after surgery. n = 3-5 per group.

(C) The numbers of $CCR8^+$ Treg cells (Left) and total Treg cells (Right) in bone callus tissue on P7. n = 5 per group.

(D) The numbers of $CCR8^+$ Treg cells (Left) and total Treg cells (Right) in adjacent lymph node on P7. n = 4 per group.

(E) Frequencies of total SSC lineage cells, SSCs, BCSPs, and $Thy1^+$ cells in total Lin^- cells at the injury site on P7. n = 4-5 per group.

(F) Safranin O staining (Upper) and HE staining (Lower) of bone tissues at injury site in Cntrl, CCL1 treated group and CCR8 inhibitor-treated group on P14 and P28, respectively. Scale bars: 200μm.

(G) The Safranin O images were analyzed using Image J Ver.1.48. n = 5 per group.

(H) Representative micro-CT images showing fracture healing.

(I) Quantitative analysis of bone volume fraction (BV/TV) and bone volume of callus tissue. n = 5 per group.

All data are presented as mean ±s.e.m. *P ≤ 0.05, **P ≤ 0.01, ***P ≤ 0.005, ****P ≤ 0.001, as determined by one-way ANOVA with Bonferroni multiple comparisons test.

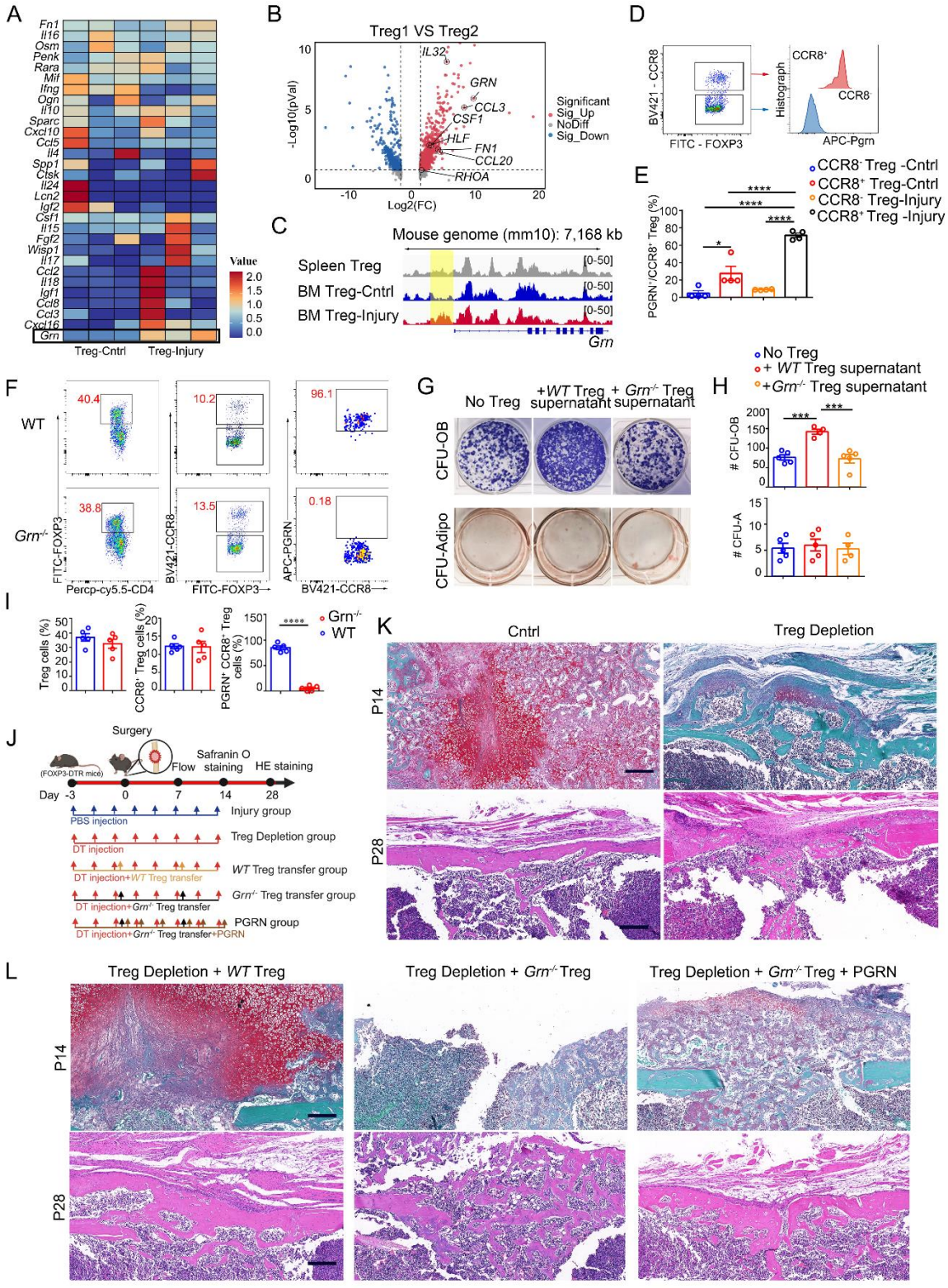

Figure 7. Bone injury-responding Treg cells display bone repair function dependent on secretion of PGRN

(A) Heatmap showing the expression of secreted factors in Treg cells at injury site and Treg cells in the control bone marrow. n = 3 per group.

(B) Volcano plots representation of a comparison of secreted genes expression profiles between Treg1 subset and Treg2 subset.

(C) Chromatin accessibility of the *Grn* locus in spleen Treg cells, bone marrow Treg cells in control and injury group.

(D) Representative images of the expression of PGRN in $CCR8^+$ Treg cells and $CCR8^-$ Treg cells.

(E) Quantification of the expression of PGRN in $CCR8^+$ Treg cells and $CCR8^-$ Treg cells. n = 4 per group.

(F) Representative images showing the percentage of total Treg cells, $CCR8^+$ Treg cells and $PGRN^+CCR8^+$ Treg cells in *WT* mice and $Grn^{-/-}$ mice.

(G) Representative images of colonies of osteogenic (CFU-OB) and adipogenic (CFU-Adipo) assays showing the effect on the control with no Treg conditioned medium, with *WT* Treg conditioned medium and with $Grn^{-/-}$ Treg conditioned medium.

(H) Quantification of CFU-OB and CFU-Adipo colonies. n = 4-5 per group.

(I) Statistical analysis of the proportions of Treg cells in $CD4^+TCR\beta^+$ cells, the proportion of $CCR8^+$ Treg cells among total Treg cells, and the percentage of $PGRN^+CCR8^+$ Treg cells in $CCR8^+$ Treg cells in *WT* mice and $Grn^{-/-}$ mice. n = 5 per group.

(J) Diagram of the experimental protocol showing the transfer of *WT*/ $Grn^{-/-}$ Treg cells into Treg-depletion mice after injury.

(K-L) Safranin O staining of bone tissues on day 14 after injury operation (Upper). HE of bone tissues on day 28 after injury operation (Lower). Scale bars: 200μm.

All data are shown as mean ±s.e.m. *P ≤ 0.05, ***P ≤ 0.005, ****P ≤ 0.001, as determined by one-way ANOVA with Bonferroni multiple comparisons test (E, G) or unpaired two-tailed Student's t-test (H).

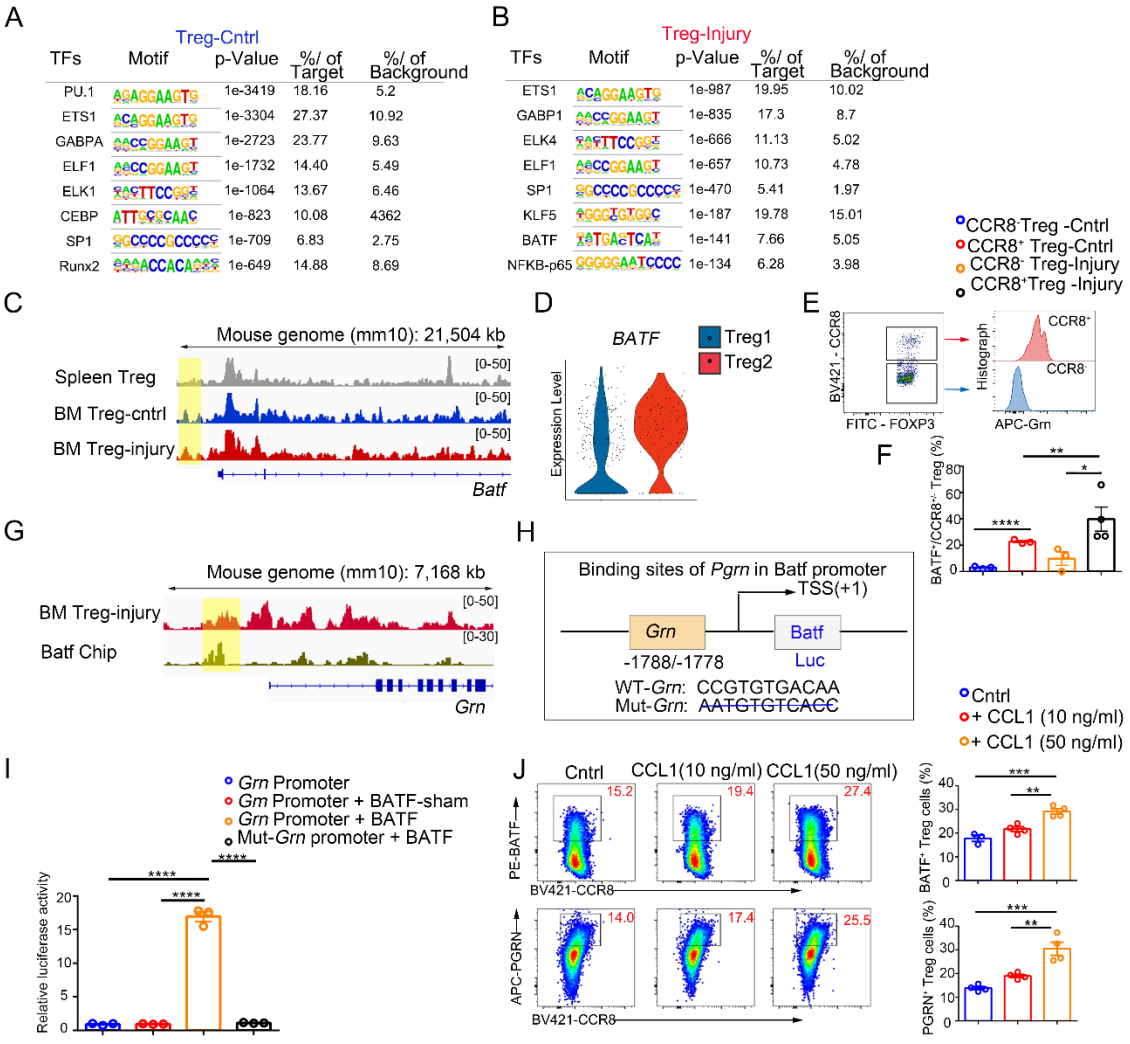

Figure 8. BATF modulates PGRN expression in the injury-responding Treg cells.

(A) De novo motif-enrichment analysis of ATAC-seq peaks associated with Treg-Cntrl cells expressed genes encoding transcription factors. Random background regions serve as a control.

(B) De novo motif-enrichment analysis of ATAC-seq peaks associated with Treg-Injury cells expressed genes encoding transcription factors. Random background regions serve as a control.

(C) Chromatin accessibility of the *Batf* locus in spleen Treg cells, bone marrow Treg cells

in control and injury group.

(D) Violin plot showing the expression level of *BATF* in Treg1 subset and Treg2 subset.

(E) Representative images of the expression of BATF in $CCR8^+$ Treg cells and $CCR8^-$ Treg cells.

(F) Quantification of the expression of BATF in $CCR8^+$ Treg cells and $CCR8^-$ Treg cells. n = 3 per group.

(G) Chromatin accessibility of the *Grn* locus in bone marrow Treg cells with BATF ChIP-Seq data.

(H) Diagram graph showing the binding sites of *Grn* with *Batf*.

(I) Dual luciferase reporter assay in HEK293A cells co-transduced with luciferase reporter driven by wild-type or mutant *Grn* pomoter and expression plasmid of *Batf*. n = 3 per group.

(J) Representative images and quantification of $BATF^+$ and $PGRN^+$ $CCR8^+$ Treg cells with or without treatment with CCL1 (10 ng/ml or 50 ng/ml). n = 3-4 per group.

All data are shown as mean ±s.e.m. *$P \leq 0.05$, **$P \leq 0.01$, ***$P \leq 0.005$, ****$P \leq 0.001$, as determined by one-way ANOVA with Bonferroni multiple comparisons test.